Synthesis and characterization of amorphous-nanocrystalline Fe$_{70}$Cr$_{10}$Nb$_{10}$B$_{10}$ powders by mechanical alloying

Baris Avar[1] · Arun K. Chattopadhyay[2] · Tuncay Simsek[3] · Telem Simsek[4] · Sadan Ozcan[4,5] · Bora Kalkan[6,7]

Abstract

In this study, structural, morphological, thermal and magnetic properties of amorphous-nanocrystalline Fe$_{70}$Cr$_{10}$Nb$_{10}$B$_{10}$ (at.%) alloy are discussed. The formation and evaluation of amorphous-nanocrystalline structures of the alloy were followed by XRD, SEM-EDX, TEM, DTA, and VSM techniques. After 50 h of milling Cr, Nb, and B were completely dissolved into the Fe lattice forming 82% of the amorphous phase of the alloy. A gradual dissolution of the alloying elements also increased the lattice parameters concurrently. The lattice parameters reached a maximum value of 2.908 Å after 20 h of milling and then leveled off to a value of 2.891 Å at the end of 50 h of milling. Based on the XRD data, crystallite size and lattice strain of the alloy were calculated as 3.2 nm and 3.34% respectively. TEM analyses revealed that the alloy particulates comprised needle-shaped nanoparticles of an average size of 21 nm. The room temperature magnetic hysteresis loops showed that the increased duration of milling decreased the saturation magnetization from 91 to 24 emu/g. This was mainly due to the upsurge on the amorphous phase content in the alloy as the milling progressed. The increase in amorphous phase content and the subsequent reduction of the saturation magnetization were due to the inter-diffusion of the non-ferromagnetic Cr and B atoms into the Fe lattice. Thermal studies revealed that around 350 °C the amorphous phase of the alloy began crystallizing. The magnetic saturation of the heat-treated alloy also increased with the growth in the crystalline phases. The 50 h milled sample annealed at 700 °C was found to have the highest magnetic anisotropy as observed from the temperature-dependent zero-field cooled and field cooled magnetization measurements. The high-pressure X-ray diffraction measurements revealed that the amorphous state of the alloy remained stable up to 11.3 MPa. It also revealed the structural similarities of the Fe$_{70}$Cr$_{10}$Nb$_{10}$B$_{10}$ alloy with those of the Fe$_{70}$M$_{10}$B$_{20}$ (M=Nb and Cr) types. For all practical purposes, the microstructural stability under high compressive pressure represents the consolidation properties of the nanostructured magnetic materials since both pressure and temperature-induced phase transformations are the primary controlling factors for the specific magnetization properties of the alloy.

Keywords Amorphous structures · Nanocrystals · Mechanical alloying · Soft magnetic materials

✉ Tuncay Simsek
tuncaysimsek@kku.edu.tr

Baris Avar
barisavar@beun.edu.tr

Arun K. Chattopadhyay
akchatto@gmail.com

Telem Simsek
telem@hacettepe.edu.tr

Sadan Ozcan
sadan@hacettepe.edu.tr

Bora Kalkan
bkalkan@ucsc.edu

[1] Department of Metallurgical and Materials Engineering, Zonguldak Bülent Ecevit University, 67100 Zonguldak, Turkey

[2] Uniformity Labs, Fremont, CA 94538, USA

[3] Department of Mechanical and Metal Technologies, Kırıkkale University, 71450 Kirikkale, Turkey

[4] Institute of Science, Nanotechnology and Nanomedicine Division, Hacettepe University, 06800 Ankara, Turkey

[5] Department of Physics Engineering, Hacettepe University, 06800 Ankara, Turkey

[6] Advanced Light Source, Lawrence Berkeley National Laboratory, Berkeley, CA 94720, USA

[7] Earth and Planetary Sciences Department, University of California, Santa Cruz, CA 95064, USA

1 Introduction

Fe-based amorphous-nanocrystalline alloys are of great importance in many commercial applications such as power systems, motors, sensors, transformers, etc. due to their remarkable soft magnetic properties such as effective permeability and saturation magnetic flux density [1–4]. During the last few years, the thrust for exploring and developing new nanocrystalline soft-magnetic alloys has increased significantly because of increasing demands for soft-magnetic materials that require both high induction and permeability including good mechanical properties and corrosion resistance. For that matter, nanocrystalline alloys comprising α-Fe nanocrystalline phases are particularly important for the advancement of soft magnetic materials with improved properties. As opposed to the conventional magnetic alloys, the nanocrystalline alloys generally have dual-phase structures composed of soft ferromagnetic amorphous matrix and ferromagnetic body-centered cubic (bcc)-Fe type nanocrystalline phases. An improvement in soft magnetic properties in nanocrystalline magnetic alloys is primarily embedded in the orderly distribution of fine crystalline grains within an amorphous matrix. In addition to that, by altering alloy chemistry and the method of manufacturing, a wide range of magnetic materials can be produced with desired combinations of physical and magnetic properties required for a particular operation.

In general, the Fe-based nanocrystalline soft magnetic alloys can be described as $Fe_{(1-x)}(T, M, and NM)_x$, where T is an early transition metal element, M is a metalloid, and NM is a noble metal [1]. Each component of the composition serves specific purposes to bring about the desired material properties. For example, the addition of an early transition metal (T = Zr, Nb, Hf, Ta, etc.) and a metalloid (M = B, P, Si, etc.) is to form glass as a precursor amorphous alloy phase, and the presence of a noble metal element (NM = Cu, Ag, Au, Rh, Ru, Os, Pd, etc.) is for promoting nucleation of the ferromagnetic nanocrystalline phase [1].

In this context Fe-M-B (M = Zr, Si, Hf, Nb, etc.) type of alloys can be referred for high saturation magnetic flux densities and superior soft magnetic properties, which has a structure consisting of nanoscale bcc grains with a small amount of intergranular amorphous layers. The superior soft magnetic properties observed in these alloys are achieved through controlled crystallization of their amorphous phases [5]. The first alloy of that kind was developed almost two decades ago. It was made by melt-spinning of Fe-Si-B alloys containing small amounts of Nb and Cu. The amorphous form of Fe-Si-B-Nb-Cu alloy was then annealed above its crystallization temperature to form α-Fe nano-grains of body-centered cubic (bcc) Fe-Si [3]. However, the major drawback of the melt-spinning technique was, that the end products were in the form of flakes or ribbons, and that was why they were not very suitable for producing bulk alloy forms [6]. It is indeed very important in this regard that due consideration must be given to the processing routes and methods for controlling the alloy chemistry. The synthesis of amorphous and nanocrystalline alloys requires two primary considerations, (1) alloy design and (2) an expedient selection of the processing method to produce alloys in the amorphous state. For larger-scale productions of alloys, the synthetic routes that are considered viable, are: (1) Powder synthesis techniques, (2) Rapid solidification processing, (3) Solidification processing of bulk amorphous alloys, and (4) Crystallization of amorphous precursors [1, 6]. Despite having several routes and methods of synthesis, to achieve an industrial-scale production, the powder production route is seemingly the most workable one for accomplishing the objective. In this respect mechanical alloying (MA) techniques are seemingly very effective for the bulk production of the alloy powders. MA techniques are already in use for the production of amorphous and nanocrystalline alloys. The powder forms of the alloys produced by MA can be easily consolidated into bulk shapes, and their desired microstructural properties for commercial application can be achieved by annealing. Furthermore, MA is of great interest recently due to its simplicity, relatively low equipment cost, and versatility in synthesizing various groups of materials including nanocrystals, amorphous materials, quasicrystals, and intermetallic compounds, and solid solutions. The ease of controlling several synthesizing parameters, such as ball-to-powder weight ratio (BPR), milling speed and durations, process control agent and milling atmosphere, etc., is the most tangible advantage of using the MA technique for the production of nanocrystalline alloys [7–14]. During the last couple of decades, considerable efforts have been made in designing amorphous and nanocrystalline alloys similar to Fe-Nb-B type exploiting MA routes. For instance, Cao et al. [15] reported thermally stable nanocrystalline phase formation of $Fe_{84}Nb_7B_9$ alloy powders after 96 h of milling. That alloy had good thermal stability up to 770 °C. Sunol et al. [16] examined the $Fe_{72.5}Co_{7.5}Nb_{(5+x)}B_{(15-x)}$ ($x = 0$, 5, and 10 at.%) alloys during the MA process, and showed that the substitution of B with Nb increased the thermal stability of the nanocrystalline powders. Chabi et al. [4] also studied the effect of B content on the amorphization process and on the structural, morphological, and magnetic properties of the ball-milled $Fe_{(92-x)}Nb_8B_x$ ($x = 5$, 10, 15, and 20) powders. According to their investigation, the amorphous phase fraction of the alloy was

increased by increasing B content in the formulation, which in turn resulted in decreased magnetic saturation (M_s) and increased coercivity (H_c) of the alloy. Slimi et al. [17] recently reported the formation of nanocrystalline fcc-Fe(Ni) and bcc-Fe(Ni,Cr) solid solutions in the mechanically alloyed $Fe_{60}Ni_{20}Cr_{10}B_{10}$ (wt.%) powders. Carrillo et al. [18] developed the $Fe_{80}Nb_7B_{12}Cu_1$ (at.%) and $Fe_{80}(NiZr)_7B_{12}Cu_1$ (at.%) nanocrystalline alloys in two different high-energy ball milling devices by milling the alloy components for 80 h. In that work, all samples exhibited soft ferromagnetic behavior at room temperature. On the other hand, $Fe_{79.7-x}Cr_xNb_{0.3}B_{20}$ ($x = 11.5–13$ at.%) powders prepared by high-energy ball milling using their glassy melt-spun ribbons as precursors, demonstrated that the Fe–Cr–Nb–B systems could be the candidates of great potential for the magnetic hyperthermia applications [19]. Consequently, depending on the alloy design and the method of synthesis employed, the mechanical and magnetic properties of an alloy may vary. This is due to the possible microstructural changes that may take place during its processing. As far as literature references are concerned, it appears that nothing has been reported so far on $Fe_{70}Cr_{10}Nb_{10}B_{10}$ (at.%) composition. Hence, the aim of the present study was to investigate the structural and magnetic characteristics of the mechanically alloyed $Fe_{70}Cr_{10}Nb_{10}B_{10}$ powders by X-ray diffraction (XRD), scanning electron microscopy with energy-dispersive X-ray spectroscopy (SEM/EDX), transmission electron microscopy (TEM) and vibrating sample magnetometer (VSM) techniques. $Fe_{70}Cr_{10}Nb_{10}B_{10}$ has also been simultaneously studied using high-pressure X-ray diffraction at room temperature to determine the influence of Fe-B and M-B bonds for the phase changes with the increasing pressure and to what extent they affect the compressibility properties of $Fe_{70}Cr_{10}Nb_{10}B_{10}$. Both thermal and high-pressure stability of the nano-magnetocrystalline alloys are very important for establishing a foundation for designing and optimizing magnetic properties of the nanostructured magnetocrystalline materials.

2 Materials and methods

2.1 Sample preparations and mechanical alloying

The powder mixture of Fe (Sigma-Aldrich, 99.9%, − 400 mesh), Cr (Sigma-Aldrich, 99.5%, -100 mesh), Nb (Sigma Aldrich, 99.8%, < 45 μm), and B (Sigma-Aldrich, 98%, < 45 μm) was put in a vial to obtain $Fe_{70}Cr_{10}Nb_{10}B_{10}$ alloy under argon atmosphere. The all-sample handling and weighing of initial powders according to the nominal composition of $Fe_{70}Cr_{10}Nb_{10}B_{10}$ were performed in an Ar-filled glovebox. Mechanical alloying experiments were conducted using a planetary ball mill equipped with 250 ml hardened steel vials and hardened steel balls. The rotating speed was fixed at 500 rpm and BPR was selected as 20:1, the same as the previous experiment [20]. For milling, 25 g of the starting powder mixture was used per vial without any process control agent (PCA). To minimize the heat generated during milling and to avoid agglomerations of powder mixtures, the device was operated for 30 min and stopped for 15 min, and then again operated in reverse rotational direction for the next 30 min and repeated likewise. The powder mixture was ball milled up to 50 h. For phase identification studies small samples of the milled powder were taken out under Ar atmosphere after 1, 3, 5, 10, 20, 30, 40, and 50 h milling intervals.

2.2 Characterizations of the mechanically alloyed samples

The phase identification of the synthesized powders was performed by X-ray diffraction (XRD) with an analytical Empyrean model diffractometer using Cu-Kα ($\lambda_{\alpha1} = 1.5406$ Å, $\lambda_{\alpha2} = 1.5444$ Å) radiation. Finely ground samples of the milled powder were placed in the silicon sample cavities with silicon plates cut parallel to the (510) axis for almost "zero" background contribution to the diffraction pattern from the sample holders. Diffraction patterns were collected in steps from 20 to 90° (2θ-range) for all samples using a continuous scan rate of 1° per minute at a step size of 0.013°. The crystallite size and the lattice strain were calculated by the Williamson-Hall method [21]. The International Centre for Diffraction Data (ICDD) powder diffraction files were used for the identification of the crystalline phases. The morphology of samples was studied by SEM (FEI Quanta FEG 450) equipped with EDX (Bruker Quantax 200), and high-resolution transmission electron microscopy (HRTEM, Jeol 2100F). ImageJ Analyzer software was used for particle size determination from the SEM images [22]. The thermal behavior of the milled powders was analyzed by differential thermal analysis (DTA) in the temperature range of 200–1150 °C under N_2 flow with a heating rate of 20 °C/min using an SII Exstar TG/DTA 7200 thermal analyzer. The magnetic properties of the milled powders were investigated using the vibrating sample magnetometer (VSM) option of the Physical Properties Measurement System (Quantum Design). The magnetic field dependence of magnetization, M(H), and the temperature dependence of the magnetization, M(T) were measured within the temperature range of 10–300 K using a 500 Oe applied field. The variation of the applied magnetic field was maintained within ± 3 Tesla. The structural stability of the amorphous alloy obtained after 50 h of milling was studied by synchrotron X-ray diffraction. In situ high-pressure angle-dispersive XRD experiments with an X-ray wavelength of 0.4132 Å

and a focused x-ray beam size of ~10×10 μm² were carried out at the beamline 12.2.2, Advanced Light Source (ALS) [23]. A four-pins symmetric diamond anvil cell (DAC) with an anvil culet size of 350 μm was used to generate high pressure. Sample chambers were formed by drilling holes with a diameter of 120 μm in Re foil that was pre-indented to 40 μm thickness. Silicone-oil, which is chemically inert and provides a hydrostatic pressure of ~20 GPa [24], has served as the pressure-transmitting medium in compression experiments. The pressure was determined by the ruby fluorescence method [25]. Diffracted X-rays were collected on a Pilatus3 S 1 M fast detector at a distance of 218.4 (±1) mm. Detector distance and orientation were calibrated using a CeO₂ standard. The diffraction images were radially integrated using the program DIOPTAS [26].

3 Results and discussion

3.1 Structural analysis

Figure 1 illustrates the XRD patterns of starting powder mixture. All characteristic peaks of the constituent elements can be seen except for B due to its amorphous structure and low atomic scattering factor [27]. Furthermore, no impurities could be identified in the powder mixture as well. Figure 2 shows the XRD patterns of $Fe_{70}Cr_{10}Nb_{10}B_{10}$ (at.%) samples collected at various milling periods, viz. 0, 1, 3, 5, 10, 20, 30, 40, 50 h of mechanical alloying. It is very apparent that the characteristic peaks of the Fe (cubic, Im-3 m, ICDD Card No: 06-0696), Cr (cubic, Im-3 m, ICDD Card No: 06-0694), Nb (ICDD Card No: 34-0370) in Fig. 2 started disappearing from the very initial stages of milling. Within 1 h of milling, the peaks belonging to Cr, and Nb completely disappeared after 5 h of milling. Within 10 h of milling, all initial elemental peaks mostly became unobtrusive, and only the peak
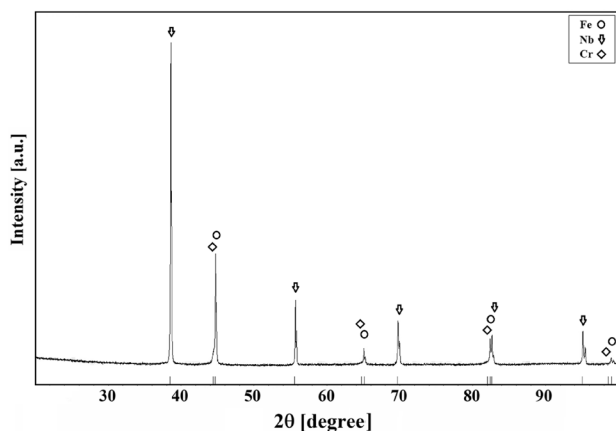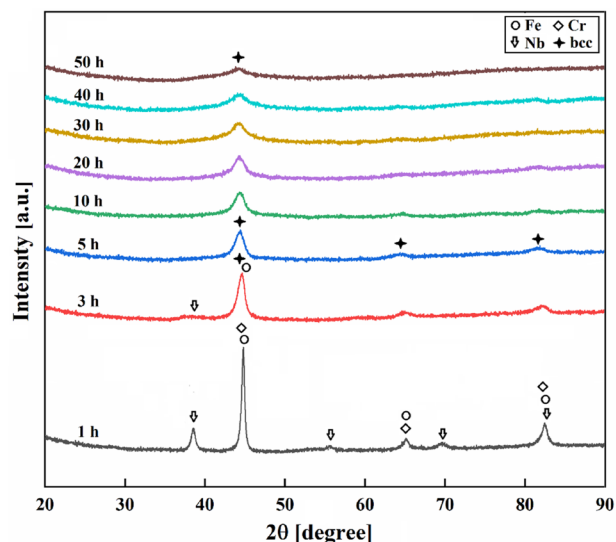

Fig. 2 XRD pattern of $Fe_{70}Cr_{10}Nb_{10}B_{10}$ alloys as a function of milling periods

for the bcc Fe(CrNbB) solid solution phase at around 44.67° became more apparent with the continuation of milling. It is also evident from Fig. 2 that the 44.67° peak intensity progressively decreased and the area beneath that peak gradually getting broadened as the milling continued. Besides an incremental dissolution of Cr, Nb, and B in the Fe lattice, this situation also indicated the reduction in the crystallite size during milling. Figure 3a illustrates an increase in the amorphous phase fractions formed after each stage of the milling. The formation of the amorphous phase is mainly through the development of microstructure initiated by the plastic deformation of the particles of the alloying elements followed by fracture and particle welding. The continuous interchanges between fracture and re-welding processes lead to the homogenization of the constituent elements, reduction of the particle sizes, and disorder in the crystal structure. As a result, in MA the particle sizes can attain a steady-state very fast whereas structural and phase modifications can continue throughout milling periods. Figure 3a–d demonstrated the structural and crystal size changes with the milling period. Therefore, as explained above, the amorphization starts due to the huge strain energy stored in the alloying mass during continuous deformations of powders causing lattice stabilizations. Also, a large thermodynamic driving force is required to generate a large negative heat of mixing during milling [28]. Inoue indicated that the formation of amorphous alloy phases with three or more alloying elements required a difference of at least 12% in atomic radii between the constituent elements, and it was also necessary to have a large negative heat of mixing (ΔH_{mix}) between the alloying elements [29]. Table 1 shows the heats of mixing (ΔH_{mix}, kJ/mol) and atomic radii of the alloying elements
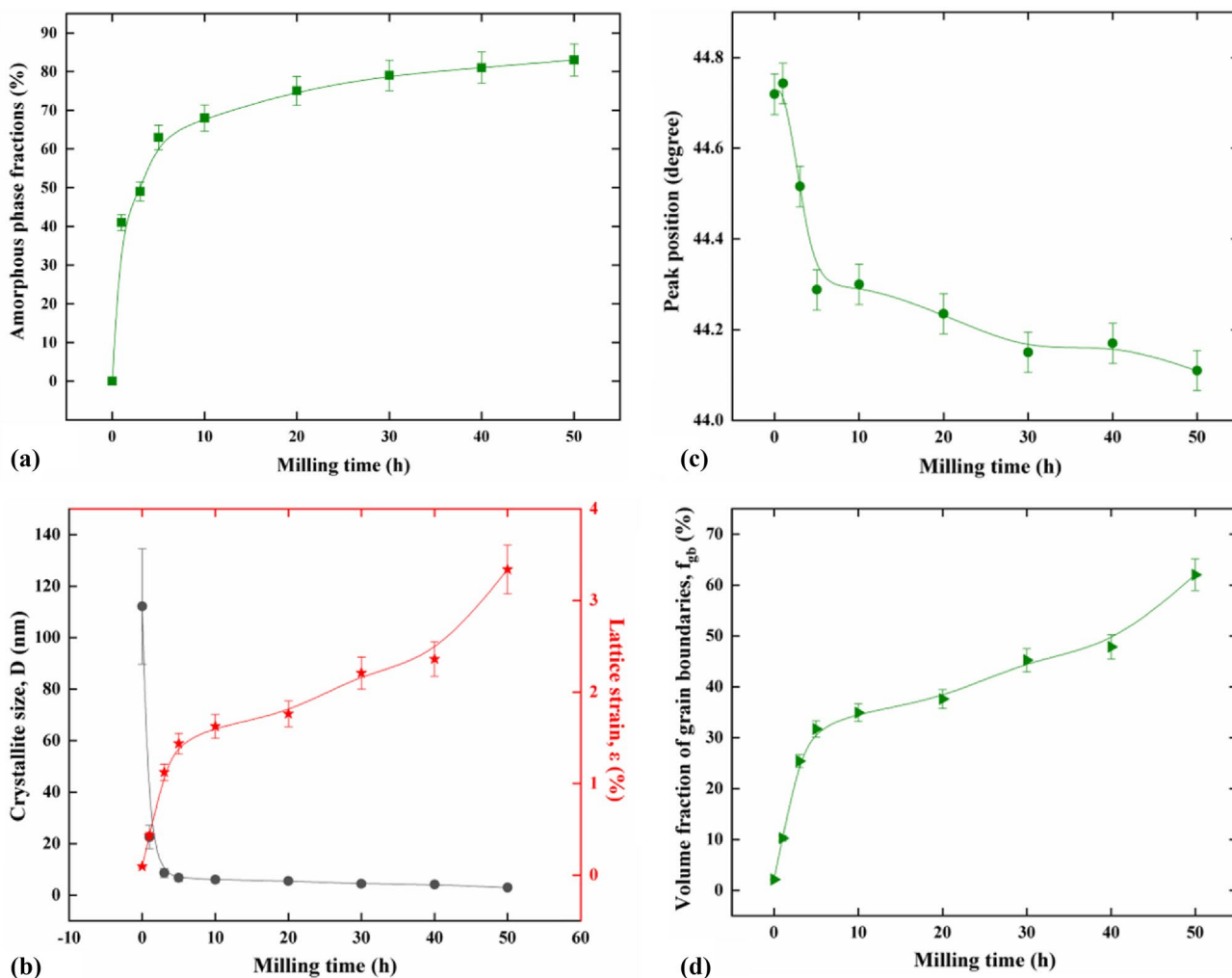

Fig. 1 XRD pattern of starting mixture

Fig. 3 **a** Amorphous phase fractions formed after each stage of milling, **b** reduction in crystallite sizes during milling, **c** gradual changes of intensity of the main peak, and **d** volume fraction of grain boundaries generated as the milling progressed from 0 to 50 h

Table 1 Heats of mixing (ΔH_{mix}, kJ/mol) among the elements, and atomic radii of different elements used in the Fe$_{70}$Cr$_{10}$Nb$_{10}$B$_{10}$ alloy [30]

Element	Atomic radius (nm)	Melting point (°C)	Fe	Cr	Nb	B
Fe	0.126	1538	–	– 1	– 16	– 26
Cr	0.128	1857		–	– 7	– 31
Nb	0.146	2468			–	– 54
B	0.90	2092				–

Fe$_{70}$Cr$_{10}$Nb$_{10}$B$_{10}$ alloy. From Table 1, it is very discernible that the big difference in atomic radii and the negative heat of mixing of the alloying elements favored the ease of formation of the amorphous phase as expected. It can be noticed that the formation of bcc single-phase solid solution along with the formation of amorphous phase occurred from the early stages of milling. The amorphous phase structures were estimated as 82% after 50 h of the milling period (Fig. 3a). Figure 3b presents the changes in the peak

position of the most intensive peak of the bcc phase. The peak position shifted to the lower angles with respect to the Fe (110) peak over a period of the first 5 h of milling. This suggests that the mechanochemical reaction between the starting materials resulted in the formation of the bcc solid solution phase. With the gradual dissolution of Cr, Nb, and B, the peak was shifted more towards lower 2θ angles. The variation of the crystallite size and lattice strains are given in Fig. 3c. The crystallite size of un-milled powders
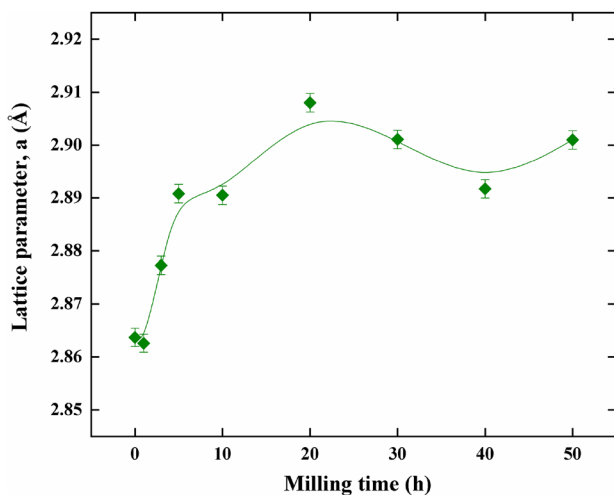
Fig. 4 Lattice parameters as a function of milling period

was calculated as 112.1 nm. It can be noticed that crystallite size decreased very sharply during the first 3 h. After that, the rate of decrease became very small and remained steady after 20 h of milling. The crystallite size was estimated as 3 nm at the end of milling. On the other hand, lattice strain was increased sharply to 1.62% up to 10 h of milling and then increased to 3.34% after 50 h of milling. Figure 4 shows the changes in lattice parameters during mechanical alloying. The lattice parameters were estimated as 2.901 Å after 50 h of milling. The lattice parameters were gradually increased to 2.908 Å up to 20 h of milling and slowly decreased to 2.891 Å after 40 h of milling. The increase in lattice parameters at the beginning of mechanical alloying

confirms the dissolution of Nb, Cr, and B in the Fe lattice to form the $Fe_{70}Cr_{10}Nb_{10}B_{10}$ alloys [31].

3.2 Morphological analysis

The SEM images of the starting powders are given in Fig. 5. As seen, Fe powders were of irregular shapes while B powders were mostly of cuboid and irregular forms. Cr and Nb particles were irregular and dense shaped. The SEM micrograph of the powder blend at various duration of mechanical alloying is illustrated in Fig. 6. Besides particle size reduction, the particle morphologies were also changed from irregular to spherical one due to the continuous fracturing, flattening, and cold-welding processes during MA. The particle size distribution given in Fig. 7 demonstrates their impacts on the particle size changes as the milling continues. The particle size was found to decrease very rapidly during the early stages of milling (Figs. 5h, 6c sample) and then there was an increase (Figs. 6d, 10h sample) due to the cold welding, which was followed by gradual reductions as the milling progressed further. Eventually, the size reduction slowly became stable, and the particles were work-hardened for the remaining part of the milling [7]. At the initial phase of milling the average particle size was calculated as 257 μm and then finally decreased to 25 μm at the end of the milling. One can see that the average crystallite size calculated from XRD is generally much lower than the particle size calculated from SEM and TEM images. The particles shown in the SEM images are bigger than their crystallite sizes. As an effect of cold welding the particles of the milled sample, as seen in the SEM images, are in the agglomerated forms of several crystallites and primary particles of the alloy [32].

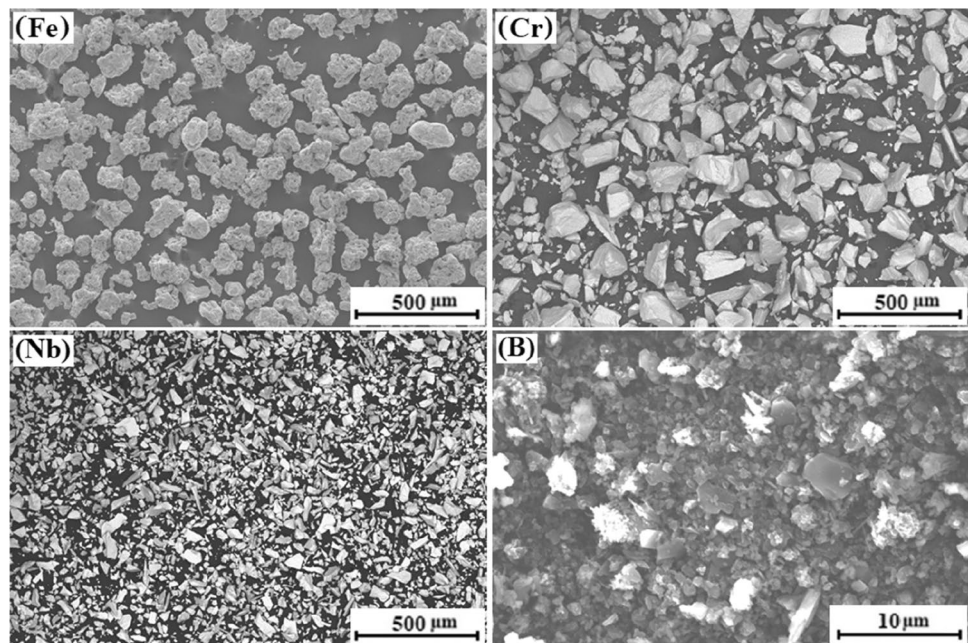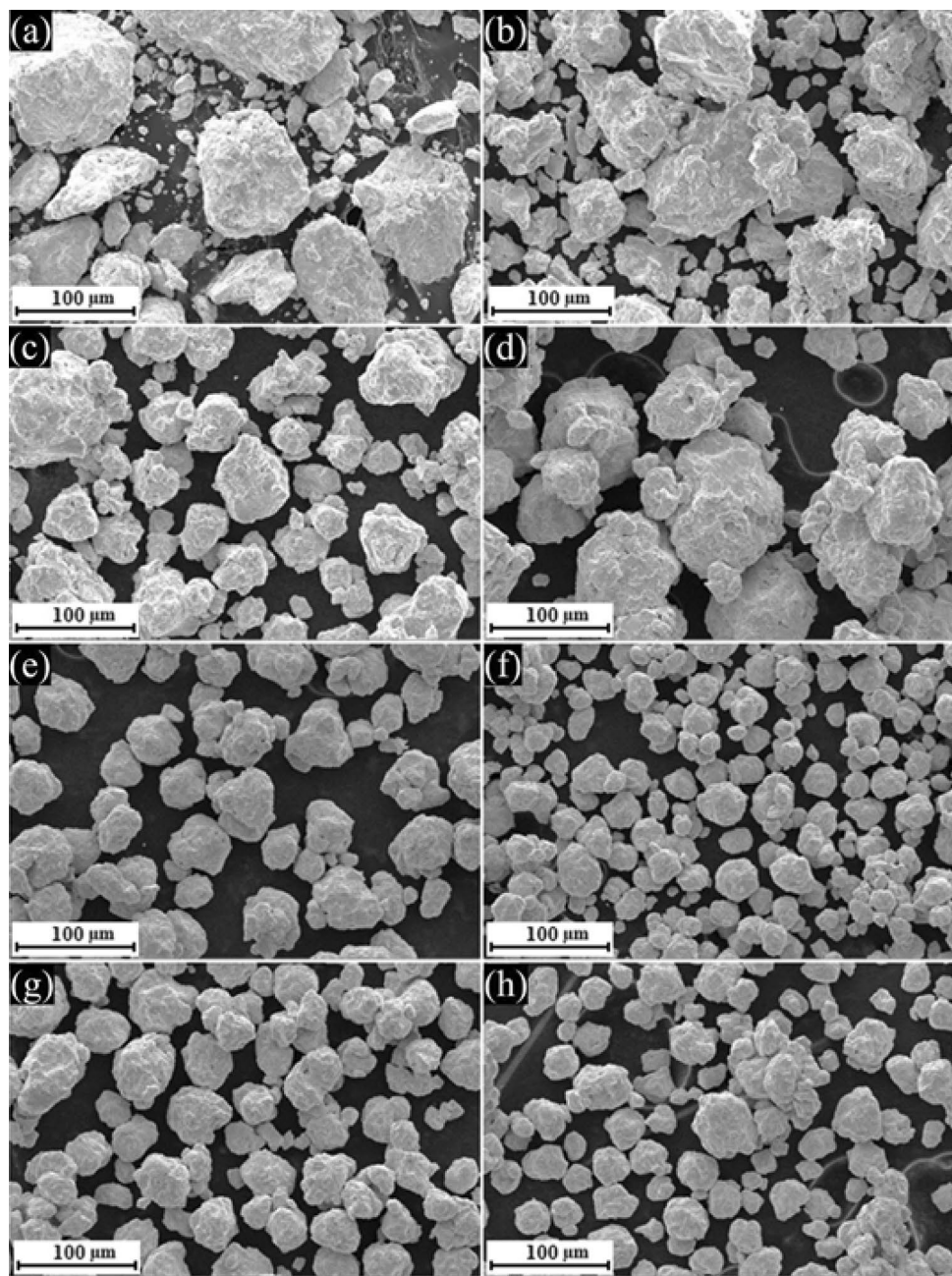**Fig. 5** SEM images of the starting powders

Fig. 6 SEM images of the powders milled at various milling period; **a** 1 h, **b** 3 h, **c** 5 h, **d** 10 h, **e** 20 h, **f** 30 h, **g** 40 h, **h** 50 h

The chemical homogeneity and purity of Fe$_{70}$Cr$_{10}$Nb$_{10}$B$_{10}$ were analyzed with EDX analysis. The SEM-EDX elemental mappings revealed the homogenous distribution of Fe, Cr, Nb, and B in the alloy. EDX analysis in Fig. 8 showed no peaks of any undesired elements in the alloy.

The TEM analysis was performed for a detailed analysis of the individual particle morphology of the alloy. Figure 9 presents the high-resolution TEM images of a 50 h milled sample of Fe$_{70}$Cr$_{10}$Nb$_{10}$B$_{10}$ alloy. TEM revealed the presence of 10–80 nm needle-shaped crystallites in the agglomerated alloy clusters.

Figure 10 presents the XRD patterns of 50 h samples of (i) as-milled powder, (ii) milled powder annealed at 350 °C, and (iii) milled powder annealed at 700 °C. As seen, 50 h as-milled sample was composed of bcc and amorphous phases. The XRD pattern of the sample annealed at 350 °C showed the imminent signs of crystalliza-tion. The peak intensity was increased and the peak area beneath was broadened. Furthermore, when the powder sample was annealed at 700 °C, the XRD of the powder indicated that the powder was almost crystalline with a greatly diminished presence of the amorphous phases. The
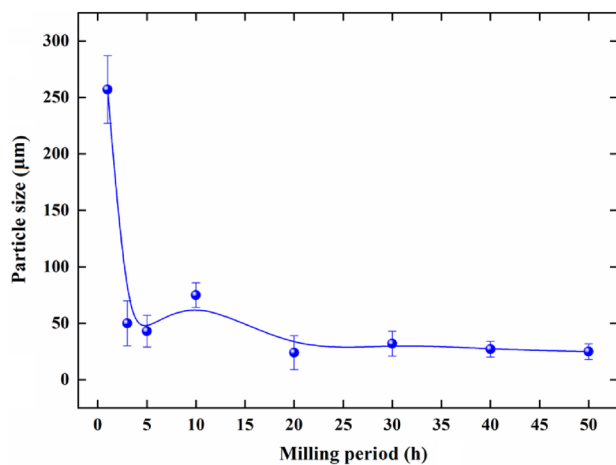
Fig. 7 Particle size distribution dependence to milling time

thermal instability of the amorphous phase of the alloy is a very useful indicator to control the kinetics of crystallinity, which can greatly influence the magnetic properties of the alloys.

3.3 Magnetic analysis

Figure 11a presents the room-temperature studies of the applied magnetic field dependence of magnetization (M(H)) loops for the alloy samples collected at milling durations of 5, 30, and 50 h. The hysteresis loops of these samples were also compared to the 50 h sample after annealing at 350 °C and 700 °C. The inset of the figure shows the enlarged loops around the zero applied field. The saturation magnetization (M_s) and coercivity (H_c) values extracted from the M(H) curves are plotted in Fig. 11b. All samples reached saturation easily with low H_c (≤ 79 Oe) and showed soft ferromagnetic behavior. As seen in Fig. 11b, as the milling time increases from 5 to 50 h, there is a rapid decrease in the saturation magnetization from 91 to 24 emu/g. As confirmed from the XRD patterns and as explained above, the non-ferromagnetic Cr and B atoms undergo interdiffusion into the lattice of the bcc α-iron phase. Magnetically α-Fe is ferromagnetic below 780 °C, its Curie temperature. As the milling continues, the increased solubility of Cr and B in the α-Fe can reduce the M_s significantly [33, 34]. The observed increase in the amorphous structure with the increasing milling time causes the disordered arrangements of the atoms resulting in a decrease in the M_s. Furthermore, the increasing surface spin disorder of the samples as a result of the size reduction further decreases the M_s [35, 36]. Therefore, because of all of these effects, there is a significant overall reduction in the M_s. However, as shown in Fig. 10, the crystallinity of the sample increased with the heat treatment. As a result, the M_s of the heat-treated sample was also increased

with the increase in crystallinity and it ascended to its highest value similar to that of the 5 h milled sample.

Figure 12 shows the temperature-dependent magnetization M(T) curves of the samples. In these experiments, at first, the temperature was lowered to 10 K without applying a magnetic field (Zero Field Cooled, ZFC). A 500 Oe external field was applied at 10 K and magnetization of the sample was measured as a function of increasing temperature. When the system reached 300 K, the sample temperature was lowered again to 10 K under an applied field of 500 Oe (Field Cooled, FC) and the magnetization was measured. In the ZFC/FC curves magnetization was continuously decreased with the rise in temperature demonstrating the ferromagnetic behavior of the samples at 300 K. It is worth mentioning that the Curie Temperature of the samples are well above the room temperature. It is also important to note that in ZFC/FC plots the temperature at which bifurcation between the ZFC/FC plots are observed, is called thermo-magnetic irreversibility temperature (T_{irr}) [37]. The 50 h sample annealed at 700 °C shows much higher T_{irr} compared to the 50 h sample annealed at 350 °C and also the 50 h as-milled sample. These results clearly show the evidence that the sample annealed at 700 °C is of higher magnetic anisotropy indicating that a uniaxial magnetic anisotropy is probably predominant in each nano-crystallite of the annealed alloy. From these results, it becomes very apparent that probably more understanding is required to generate about how the shapes, sizes, and interparticle interactions of the crystallites influence the magnetic properties of the nanocrystalline alloys.

3.4 High-pressure characterization

Figure 13a shows XRD patterns of 50 h ball milled sample of $Fe_{60}Nb_{20}Cr_{10}B_{10}$ (at.%) alloy in Q-space upon compression to ~15 GPa. Under almost ambient conditions, the nanoparticles show broad features in comparison to those observed in sample ball milled for 1 h and exhibit an amorphous-like structure with a broad contribution from the bcc crystalline phase. In agreement with our previous results, this partially crystalline structure contains a high number of bcc-Fe nanocrystals with an average size of 50 nm embedded in the amorphous matrix. The first sharp diffraction peak (FSDP), located at Q~0.83 Å^{-1} in the ambient XRD pattern (Fig. 13a) signifies intermediate range order (IRO) at a length scale of ~7.6 Å. As the pressure is increased, the FSDP shifts to higher Q values and loses its intensity, and finally disappearing ~1.1 GPa. The intensity of the principal peak (PP) located at ~3.06 Å^{-1} decreases with increasing pressure and its position shifts to higher Q values. A closer look at the pressure dependence of the PP position shows the presence of two pressure regimes. The PP position increases to higher Q with pressure with a slope of ~
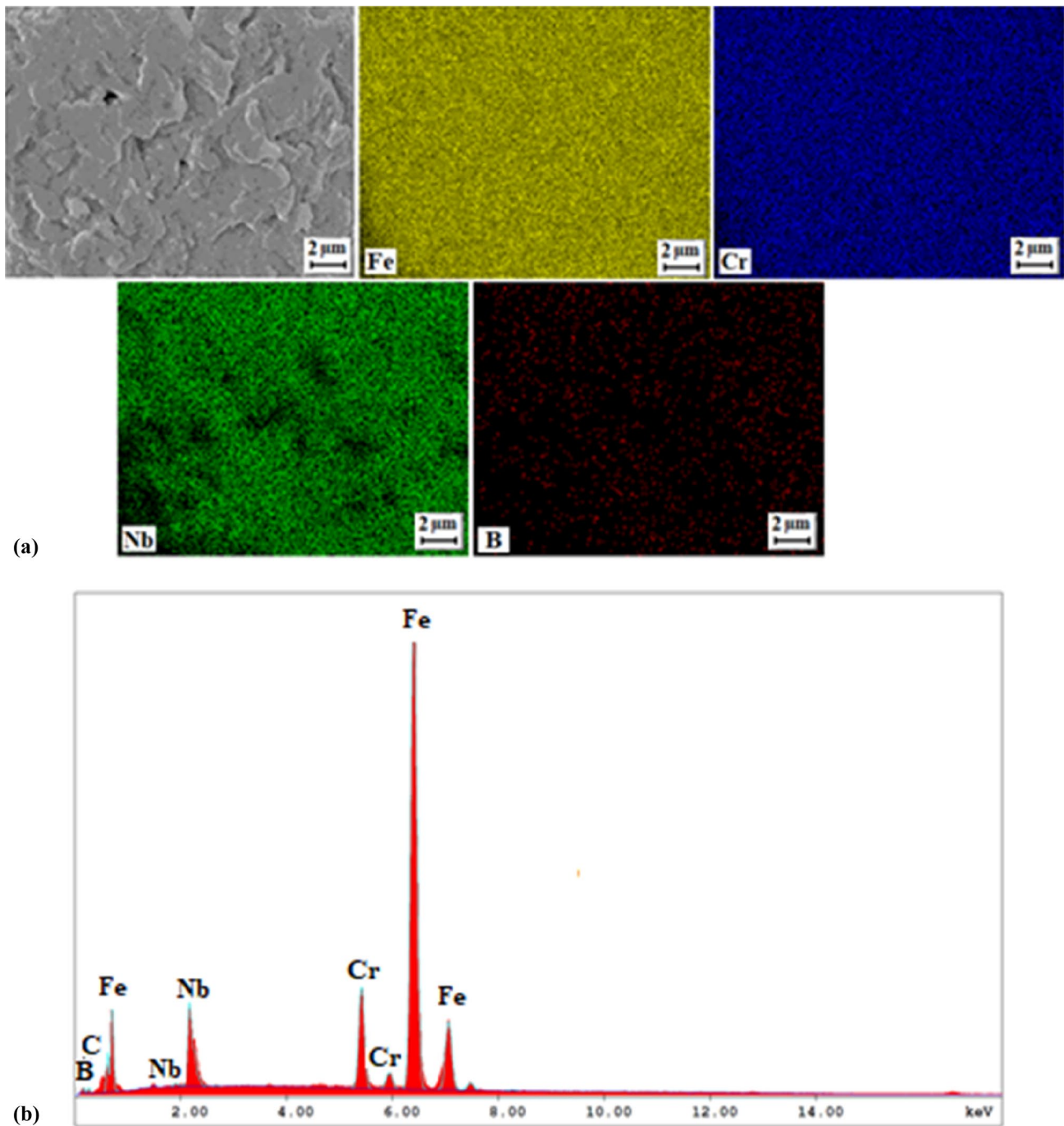
(a)

(b)

Fig. 8 **a** Elemental mapping and **b** EDX analysis of 50 h milled Fe$_{70}$Cr$_{10}$Nb$_{10}$B$_{10}$ alloy

0.004 ± 0.001 Å^{-1} GPa^{-1} in the low-pressure regime below ~ 12 GPa whereas a faster rate of increase with a slope of $\sim 0.030 \pm 0.002$ Å^{-1} GPa^{-1} is observed at higher pressures (Fig. 13b).

Based on the experimental XRD patterns, the evolution of the reduced total atomic pair distribution functions, G(r), is shown in Fig. 13c. The first peak is centered at ~ 2.4 Å, which is in good agreement with the nearest neighboring distances of Fe-B and M-B (M = Nb and Cr) pairs in amorphous Fe$_{70}$M$_{10}$B$_{20}$ alloys [38, 39]. The shoulder of the first peak located at a larger r-value (~ 3.0 Å) is attributed to the first near neighbor pairs of Fe and Nb, and Fe and Cr elements [38, 39]. Figure 13c plots shows unphysical ripples below ~ 2 Å which can be attributed to Fourier transform truncation caused by the finite range of Q measured. The atomistic origin of G(r), and direct understanding of

Fig. 9 TEM images of 50 h milled $Fe_{70}Cr_{10}Nb_{10}B_{10}$ alloy
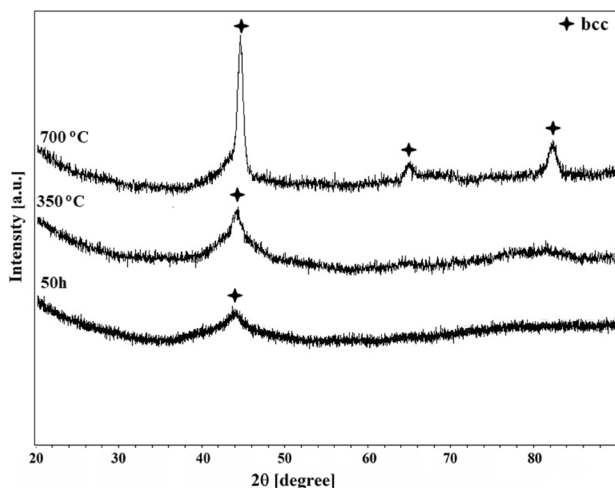
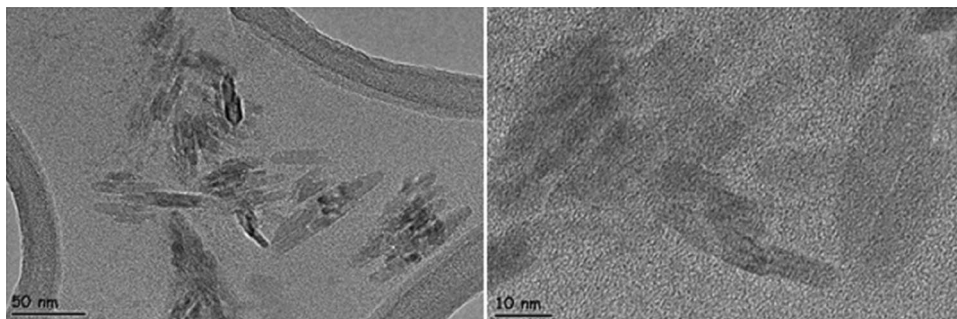**Fig. 10** XRD patterns of 50-h milled and heat-treated sample of $Fe_{70}Cr_{10}Nb_{10}B_{10}$ alloy at 350 and 700 °C

the short and medium-range structural aspects still remain unclear since the major descriptor for the atomic structure of the studied amorphous phase is still missing. This requires a study of a combination of state-of-the art high energy X-ray diffraction (such as anomalous scattering) and 3D Monte Carlo structural modeling, which would be the main topics of future research. The pressure dependence of the nearest-neighbor distances taken from the first- and second- peak positions in G(r) for Fe-B and M-B, and Fe-M (M = Nb and Cr) correlations are shown in Fig. 13d. The most salient feature observed is that the pressure changes in the first- and second-peak positions greatly differ from each other. The first peak decreases monotonically over the entire pressure range. On the other hand, the second peak position increases in the pressure range of 0–2 GPa, and then remains almost unchanged. These results suggest that the structural motifs hosting Fe-B and M-B bonds are the units dominating the compression mechanism. In [26], it's suggested that the
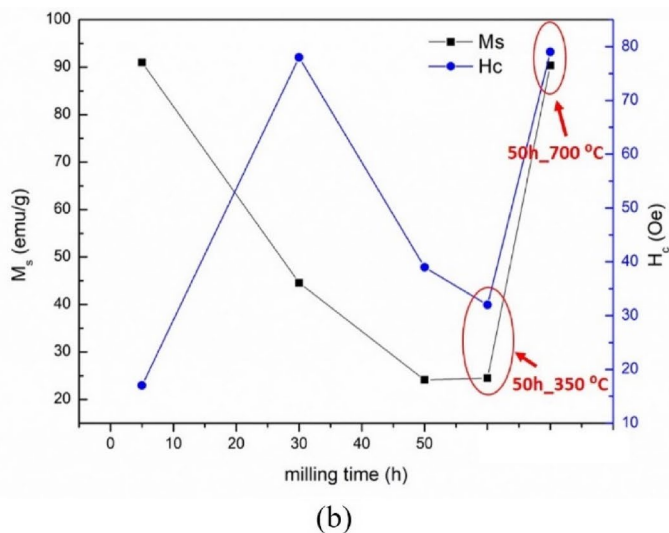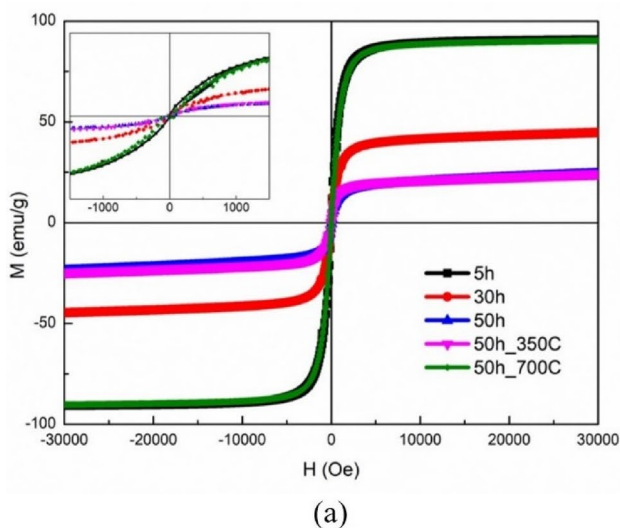

Fig. 11 **a** M(H) curves of the samples measured at 300 K. **b** M_s and H_c values extracted from M(H) curves (lines are inserted for guide to the eye)
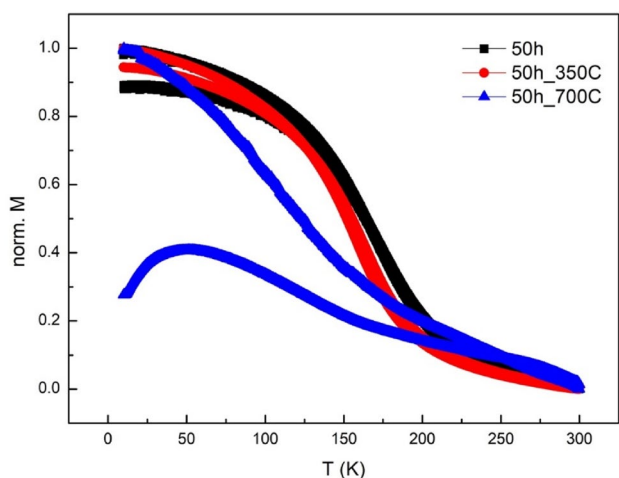
Fig. 12 ZFC–FC curves of the sample milled for 50 h and after post-annealing at 350 and 700 °C (applied field is 500 Oe)

local structural unit in the amorphous counterparts, such as Fe$_{70}$M$_{10}$B$_{20}$ (M = Zr, Nb, and Cr) alloy, is like a triangular prism, which is composed of a B atom at the center and six Fe atoms at the vertices, and M elements randomly replace Fe atoms at the vertices of the prism. Fe-M bonding is correlated with the connection between the prisms [26, 39].

For Fe$_{70}$Cr$_{10}$Nb$_{10}$B$_{10}$ alloy powders with 85% amorphous matrix where nanocrystalline bcc FeCr, bcc Nb(B), tetragonal Fe$_2$B, and orthorhombic Fe$_3$B type phases are likely to be embedded to some extent with the amorphous phase. A thermal exposure during the heat-treatment gives rise to the primary crystallization of α-Fe in addition to bcc FeCr, orthorhombic FeB, tetragonal Fe$_2$B, Fe$_3$B, and NbB type borides. The presence of Nb in the alloy powder enables microstructure modification of the alloy to excel its magnetic behavior upon annealing the alloy.
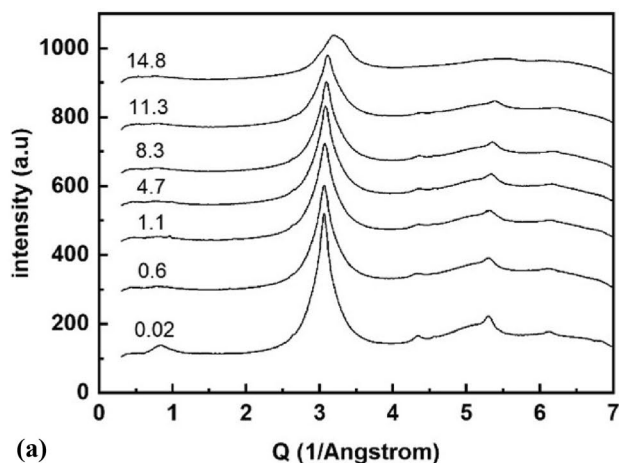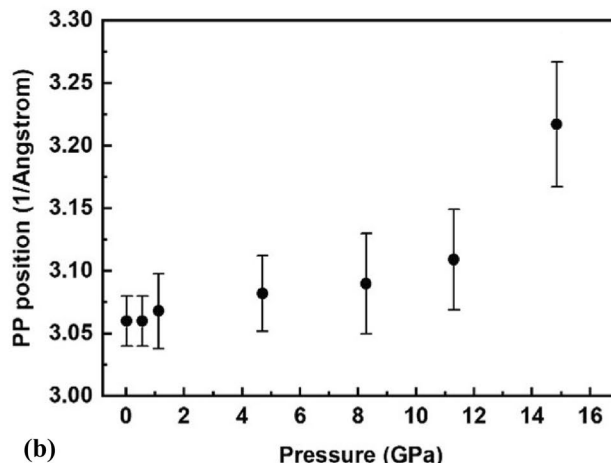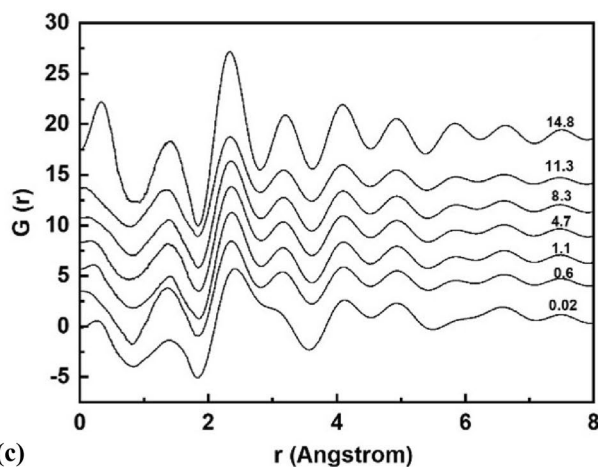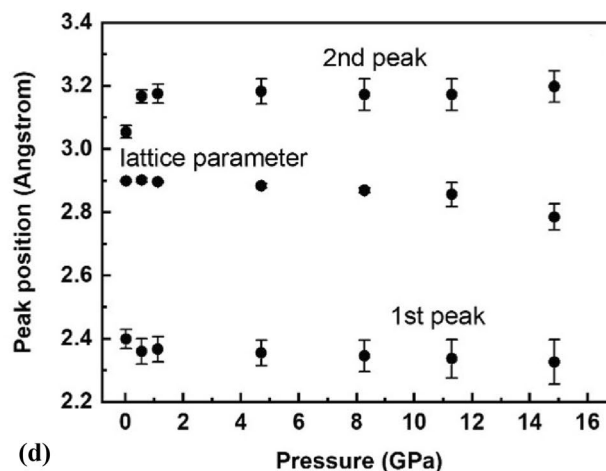

Fig. 13 **a** XRD patterns of 50 h ball milled sample up to ~ 15 GPa, **b** pressure dependence of the principal peak position in XRD patterns, **c** corresponding reduced total atomic pair distribution functions, **d** the pressure dependence of the first and second nearest-neighbor distances determined from the G(r), during compression, and the pressure dependence of bcc phase lattice parameter

4 Summary and conclusions

In this work, nanostructured $Fe_{70}Cr_{10}Nb_{10}B_{10}$ (at.%) alloy, a partial mixture of 85% amorphous phase is achieved by milling elemental Fe, Cr, Nb, and B powders for 50 h. Under ambient conditions, the alloy exhibited an amorphous-like structure from the very early stages of milling with a broad contribution from the bcc solid solution phase. With an extended milling for 50 h, the milled sample becomes more amorphous leading to a significant decrease in the saturation magnetization. After 50 h of milling the crystallite size and lattice strain of the alloy reached 3 nm and 3.34% respectively. SEM and EDX analysis revealed high purity of the alloy comprising agglomerated irregular particles. The amorphocity of the as-synthesized alloy showed instability after annealing the samples at 350 ℃. However, the amorphous phase of the alloy was completely transformed into a crystalline phase upon annealing at 700 ℃. The high-pressure X-ray diffraction measurements and real space distribution functions revealed that the local structure of $Fe_{70}Cr_{10}Nb_{10}B_{10}$ nanoparticles has similarities with its counterparts $Fe_{70}M_{10}B_{20}$ M (M = Nb and Cr) alloys, and the structural compression is dominated by Fe-B and M-B bonds in the studied pressure range of 0–15 GPa. The amorphous phase of the alloy is seemingly resilient from undergoing any major structural changes up to 11.3 GPa, which is indicative of its good compressive stability for the purpose of consolidation and material processing.

Author contributions BA: performed the experiments, data analysis, writing the first draft of manuscript, reviewing. AKC: reviewing, data analysis, editing, writing. TS: performed the experiments, data analysis, writing the first draft of manuscript, reviewing, supervision. TS: data analysis and magnetic experiments. SO: supervision and editing. BK: reviewing, editing, writing.

Data availability The datasets generated during and/or analysed during the current study are available from the corresponding author on reasonable request.

Declarations

Conflict of interest The authors declare that they have no known competing financial interests or personal relationships that could have appeared to influence the work reported in this paper. Within 3 year time frame, there is no any related interest that must be disclosed as influencing the submitted work.

References

1. M.E. McHenry, M.A. Willard, D.E. Laughlin, Prog. Mater. Sci. **44**, 291–433 (1999). https://doi.org/10.1016/S0079-6425(99)00002-X

2. L.A. Dobrzański, M. Drak, B. Ziębowicz, J. Achiev. Mater. **17**, 37–40 (2006)

3. G. Herzer, Acta Mater. **61**, 718–734 (2013). https://doi.org/10.1016/j.actamat.2012.10.040

4. T. Chabi, N. Bensebaa, S. Alleg, S. Azzaza, J.J. Suñol, E.K. Hlil, J. Supercond. Nov. Magn. **32**, 893–901 (2019). https://doi.org/10.1007/s10948-018-4734-4

5. M.A. Willard, D.E. Laughlin, M.E. McHenry, D. Thoma, K. Sickafus, J.O. Cross, V.G. Harris, J. Appl. Phy. **84**, 6773–6777 (1998). https://doi.org/10.1063/1.369007

6. M. Nabiałek, Fabrication methods for bulk amorphous alloys. In: Inamuddin, R. Boddula, M.I. Ahamed, A.M. Asiri (Eds), Alloy materials and their allied applications, Scrivener Publishing, Beverly, MA, 1–25. (2020) https://doi.org/10.1002/9781119654919.ch1

7. C. Suryanarayana. In: Mechanical alloying and milling, Ser. Materials Engineering (Marcel Dekker Incorporated), 22, Marcel Dekker, New York, (2004).

8. S. Biyik, Acta Phys Pol **135**, 778–781 (2019). https://doi.org/10.12693/APhysPolA.135.778

9. S. Biyik, J. Nanoelectron. Optoelectron. **14**, 1010–1015 (2019). https://doi.org/10.1166/jno.2019.2592

10. S. Biyik, Mater. Focus **7**, 535–541 (2018). https://doi.org/10.1166/mat.2018.1513

11. O. Guler, T. Varol, U. Alver, S. Biyik, Adv. Powder Technol. **32**, 2873–2890 (2021). https://doi.org/10.1016/j.apt.2021.05.053

12. T. Şimşek, B. Avar, T. Şimşek, B. Yıldız, A.K. Chattopadhyay, Ş Özcan, Ceram. Int. **47**, 26119–26124 (2021). https://doi.org/10.1016/j.ceramint.2021.06.018

13. M. Panigrahi, B. Avar, Appl. Phys. A **127**, 967 (2021). https://doi.org/10.1007/s00339-021-05121-4

14. M. Panigrahi, B. Avar, J. Mater. Sci. **32**, 21124–21134 (2021). https://doi.org/10.1007/s10854-021-06612-z

15. L.F. Cao, M.P. Wang, X.I.E. Dan, M.X. Guo, L.I. Zhou, T.A.N. Wang, G.Y. Xu, Trans. Nonferrous Met. Soc. China **16**, 299–303 (2006). https://doi.org/10.1016/S1003-6326(06)60051-4

16. J.J. Suñol, J.M. Güell, J. Bonastre, S. Alleg, J. Alloys Compd. **483**, 604–607 (2009). https://doi.org/10.1016/j.jallcom.2008.07.212

17. M. Slimi, M. Azabou, J.J. Suñol, M. Khitouni, J.M. Greneche, J. Magn. Magn. Mater. **393**(2015), 157–164 (2018). https://doi.org/10.1016/j.jmmm.2015.05.034

18. A. Carrillo, L. Escoda, J. Saurina, J.J. Suñol, AIP Adv. **8**, 047704 (2018). https://doi.org/10.1063/1.4994144

19. H. Chiriac, N. Lupu, M. Lostun, G. Ababei, M. Grigoraş, C. Dănceanu, J. Appl. Phys. **115**, 17B520 (2014). https://doi.org/10.1063/1.4866840

20. B. Avar, T. Simsek, S. Ozcan, A.K. Chattopadhyay, B. Kalkan, J. Alloys Compd. **860**, 158528 (2021). https://doi.org/10.1016/j.jallcom.2020.158528

21. G.K. Williamson, W.H. Hall, Acta Metall. **1**, 22–31 (1953). https://doi.org/10.1016/0001-6160(53)90006-6

22. W. Rasband, *ImageJ image processing and analysis in Java* (National Institutes of Health, USA, 2014)

23. M. Kunz, A.A. MacDowell, W.A. Caldwell, D. Cambie, R.S. Celestre, E.E. Domning, R.M. Duarte, A.E. Gleason, J.M. Glossinger, N. Kelez, D.W. Plate, T. Yu, J.M. Zaug, H.A. Padmore, R. Jeanloz, A.P. Alivisatos, S.M. Clark, J. Synchrotron Rad. **12**, 650–658 (2005). https://doi.org/10.1107/S0909049505020959

24. S. Klotz, J.C. Chervin, P. Munsch, G. Le Marchand, J. Phys. D **42**, 075413 (2009). https://doi.org/10.1088/0022-3727/42/7/075413

25. G.J. Piermarini, S. Block, J.D. Barnett, R.A. Forman, J. Phys. D **46**, 2774–2780 (1975). https://doi.org/10.1063/1.321957

26. C. Prescher, V.B. Prakapenka, DIOPTAS: a program for reduction of two-dimensional X-ray diffraction data and data exploration. High Press Res **35**, 223–230 (2015)

27. S. Sharma, C. Suryanarayana, Scr. Mater. **58**, 508–511 (2008). https://doi.org/10.1016/j.scriptamat.2007.11.004

28. R.B. Schwarz, R.R. Petrich, C.K. Saw, J. Non. Cryst. Solids. **76**, 281–302 (1985). https://doi.org/10.1016/0022-3093(85)90005-5

29. A. Inoue, Acta Mater. **48**, 279–306 (2000). https://doi.org/10.1016/S1359-6454(99)00300-6

30. A. Takeuchi, A. Inoue, Mater. Trans. **46**, 2817–2829 (2005). https://doi.org/10.2320/matertrans.46.2817

31. A. Rathi, V.M. Meka, T.V. Jayaraman, J. Magn. Magn. Mater. **469**, 467–482 (2019). https://doi.org/10.1016/j.jmmm.2018.09.002

32. T. Simsek, B. Avar, S. Ozcan, B. Kalkan, Physica B **570**, 217–223 (2019). https://doi.org/10.1016/j.physb.2019.06.047

33. M.A. Nowroozi, H. Shokrollahi, J. Magn. Magn. Mater. **335**, 53–58 (2013). https://doi.org/10.1016/j.jmmm.2013.01.034

34. H. Raanaei, M. Rahimi, V. Mohammad-Hosseini, J. Magn. Magn. Mater. **508**, 166870 (2020). https://doi.org/10.1016/j.jmmm.2020.166870

35. D. Zákutná, D. Nižňanský, L.C. Barnsley, E. Babcock, Z. Salhi, A. Feoktystov, D. Honecker, S. Disch, Phys. Rev. X **10**, 031019 (2020). https://doi.org/10.1103/PhysRevX.10.031019

36. A. Pratt, L. Lari, O. Hovorka, A. Shah, C. Woffinden, S.P. Tear, C. Binns, R. Kroger, Nat. Mater. **13**, 26–30 (2014). https://doi.org/10.1038/nmat3785

37. B.N. Sahu, K.G. Suresh, N. Venkataramani, S. Prasad, R. Krishnan, AIP Adv. **8**, 056118 (2018). https://doi.org/10.1063/1.5007791

38. P. Wirginia, P. Jacek, Solid State Phenom. **203–204**, 386–389 (2013). https://doi.org/10.4028/www.scientific.net/SSP.203-204.386

39. E. Matsubara, S. Sato, M. Imafuku, T. Nakamura, H. Koshiba, A. Inoue, Y. Waseda, Mater. Sci. Eng. A **312**, 136–144 (2001). https://doi.org/10.1016/S0921-5093(00)01903-1